

Analysis of cracking at the bottom during the last stage of Kyropoulos sapphire crystal growth

Yongchun Gao^{1, a, *}, Xingang Guo², Jianwei Lu³

¹Department of Physics, College of Science, North China University of Science and Technology, Tangshan 063009, China

²School of Control Engineering, Northeastern University at Qinhuangdao, Qinghuangdao 066004, China

³Qingong College, North China University of Science and Technology, Tangshan 063009, China

^agaoyc1963@ncst.edu.cn

Abstract

In the study, the reason of cracking at the bottom is analyzed during the last stage of Kyropoulos sapphire crystal growth. The indirect reason of crystal cracking is investigated by using the numerical simulation method. Marangoni convection reinforces the main vortex near the free surface greatly and gives rise to the interface inversion, which lowers the limit thermal stress of crystal cracking. The direct reason is discussed by considering the relation of expansion coefficient between crucible and sapphire. In addition, the proper increasing of bottom heater power can suppress the interface inversion, which is beneficial to grow the perfect crystal.

Keywords

Computer simulation, Convection, Single crystal growth, Growth from melt, Sapphire

1. Introduction

Sapphire crystal is widely used as light-emitting diodes substrate, military infrared optical window, laser host material due to excellent integrated properties [1, 2]. The Kyropoulos method is one of the most promising methods to grow large size and low residual stress of single crystal due to low temperature gradient and in-situ annealing [3].

Numerical Simulation of sapphire crystal growth in recent years mainly focused on the thermal field, flow field, stress field and the shape of the crystal-melt interface [4-9]. M.H. Tavakoli *et al.* [4] found inner and internal radiation within the growth furnace influence thermal field, heat transport structure and crystal-melt interface obviously. In the paper of H.S. Fang *et al.* [5], the factors that may cause crystal cracking during Kyropoulos sapphire growth are studied, including crystal shape, thermal stress and three-dimensional effects. C.H. Xu *et al.* [6] discussed the relationship between quality of sapphire crystal and growing parameters of SAPMAC method. C. Chen *et al.* [7] predicted the effect of crucible shape during crystal growth and proposed a special crucible shape with a round shape for the outer wall and an inverted conical shape for the inner wall which can lower the maximum velocity, the temperature gradient in the melt and the convexity. Gaurab Samanta *et al.* [8] analyzed the limit points related to crystal size, pull rate and capillary effects in the micro-pulling-down system of Sapphire. W.J. Lee *et al.* [9] studied the effect of crucible geometry on melt convection and interface shape and it was concluded that the crucible with a curved bottom had advantages for the crystallization of the sapphire using the Kyropoulos method. The previous studies ignored the marangoni convection or didn't analyze its effect clearly, but the convection drove by surface tension can influence the flow field and melt-crystal interface, especially with the decreasing of the melt volume.

In this work, the effect of the marangoni convection on the flow field, thermal field and melt-crystal interface during the Kyropoulos sapphire crystal growth is investigated utilizing the CGSim program package [10].

Table 1 Physical properties used in the present system

physical properties	value
Melting point T_m (K)	2313
Density	
Crystal ρ_c (kg/m ³)	3960
Melt ρ_l (kg/m ³)	3000
Thermal conductivity	
Melt λ_l (W/mk)	3.5
Heater λ_h (W/mk)	147
Molecular heat conductivity kmol(W/mk)	3.5
Heat capacity	
Crystal $C_{p,c}$ (J/kgK)	765
Melt $C_{p,l}$ (J/kgK)	765
Thermal expansion coefficient β (k-1)	1.8×10^{-5}
Dynamic viscosity η (Pas)	0.058
Emissivity	
Crystal ϵ_c	0.9
Melt ϵ_l	0.33
Tungsten (W) crucible	0.3
Molybdenum (Mo) slices	0.28
Heater ϵ_h	0.3
Stefan-boltzman constant σ (W/m ² k ⁴)	5.67×10^{-8}
Thermocapillary coefficient dy/dT (dyn/cmK)	-3.5×10^{-2}
Absorption coefficient aR (m-1)	19.26
Refractive index	1.78

2. Model

2.1 Physical model

A stationary axisymmetric system model is used as shown in Fig.1a. The diameter of Tungsten Crucible is 125mm, the thickness of the crucible sidewall is 13mm, the thickness of the crucible bottom wall is 25mm and 35kg sapphire crystal can be grown. The heaters are divided into three regions: upper heater A, middle heater B and bottom heater C. The power ratio of three heaters is A:B:C as shown in Fig. 1a. The furnace is in high vacuum 10^{-3} Pa. Special quadrangular and matched grids in the melt and in the crystal near the crystallization front to prepare the computations of melt-crystal interface geometry. Other material blocks are meshed with triangular grids in Fig.1b. All materials defined to the blocks are assumed to be isotropic. The physical properties used in the present study are from Ref. [7] and listed in Table 1.

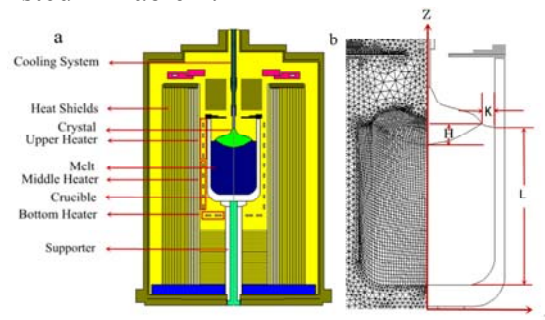


Fig.1. (a) a schematic of the KY furnace (b) meshed crystallization zone

The melt flow in a KY furnace is driven by two basic modes: natural convection due to buoyancy force and Marangoni convection due to surface tension gradient. The dimensionless parameters which are used in our paper are Grashof number and Marangoni number. The Grashof number

$Gr = g\beta(T_{max} - T_m)L^3\rho_l^2/\eta^2$ represents the strength of natural convection caused by the buoyant force. Since the strength of natural convection weakens with the volume of melt decreasing, the characteristic size L is the height of melt. T_{max} is the maximum temperature at the crucible wall and T_m is melting point. The Marangoni number $Ma = |d\gamma/dT|(T_{surmax} - T_m)K\rho_l C_{p,l}/\lambda\eta$ represents the strength of Marangoni convection caused by the surface tension. T_{surmax} is the maximum temperature of free surface. The characteristic size K is the width of free surface in the radial direction. The convexity of melt-crystal interface H is the height of the interface in the z -direction [11]. The convexity H , the characteristic sizes L and K are shown in Fig.1b.

At the free surface of melt, the boundary condition is applied, $\tau = \frac{\partial\gamma}{\partial T}\Delta T$, where $\frac{\partial\gamma}{\partial T}$ is thermocapillary coefficient. The stress τ is the driven force of Marangoni convection.

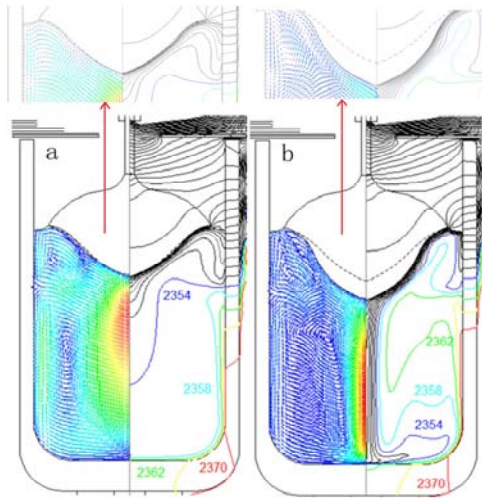


Fig.2. The flow field (left-hand side) and thermal field (right-hand side) during the shoulder turning process (the length of the grown crystal is 60mm) without (a) and with (b) Marangoni convection

2.2 Mathematical model

Recently, a two-step approach proposed by Demina *et al.* [12] is employed for heat transfer analysis: the global heat transfer in the whole system is calculated first considering all furnace elements; the heat exchange in the crystallization zone, including the crystal and melt, is then subsequently modeled separately with pre-calculated thermal boundary conditions. The validity of this numerical approach is previously verified by comparison with experimental observations in Refs. [12, 13].

2.2.1. Model of global heat exchange in the whole system

The global heat transfer of the balance equation in the whole system is written as

$$k \left[\frac{1}{r} \cdot \frac{\partial}{\partial r} \cdot \left(r \frac{\partial T}{\partial r} \right) + \frac{\partial^2 T}{\partial z^2} \right] + \dot{q} = 0, \tag{1}$$

where k is the thermal conductivity, \dot{q} is a volume source of the heat generation.

The radiative heat exchange between any solid surfaces through a non-participating medium is computed in terms of gray diffusive surface radiation. The heat-balance equation on the boundary between any solid surfaces through a non-participating medium can be written in accordance with the Stephan–Boltzman law as

$$q_k^{out} = \varepsilon_k \sigma T_k^4 + (1 - \varepsilon_k) q_k^{in}, \tag{2}$$

where \mathcal{E}_k is the emissivity, q_k^{out} and q_k^{in} are the outgoing and incoming radiation flux, respectively, and the subscript k is the cell index (the elementary surface element). The total radiative flux incoming on a given surface element is calculated using the configuration factors. In the frame work of this method, the incoming radiation flux can be calculated as

$$q_k^{in} = \sum_{j=1}^N q_j^{out} F_{kj}, \quad (3)$$

where F_{kj} is the configuration factor depending on the reactor design and the generated computational grid. The boundary of the cooling system is at constant temperature T .

2.2.2. Model of the melt convection and solidification in the crystallization zone

Then the heat exchange in the crystallization zone, including the crystal and melt is computed [14]. The external thermal boundary conditions is taken from the global heat transfer analyses. The melt is assumed to be laminar incompressible Newtonian fluid with the Boussinesq approximation and without consideration of viscous dissipation. The governing equations can be expressed as follows:

(a) Continuity:

$$\frac{1}{r} \cdot \frac{\partial}{\partial r} (r \cdot V_r) + \frac{\partial V_z}{\partial z} = 0, \quad (4)$$

(b) Momentum in the r -direction:

$$\rho \cdot \left(V_r \cdot \frac{\partial V_r}{\partial r} + V_z \cdot \frac{\partial V_r}{\partial z} \right) = -\frac{\partial P}{\partial r} + \mu \cdot \left[\frac{\partial}{\partial r} \cdot \left(\frac{1}{r} \cdot \frac{\partial}{\partial r} \cdot (r \cdot V_r) \right) + \frac{\partial^2 V_r}{\partial r^2} \right], \quad (5)$$

(c) Momentum in the z -direction:

$$\rho \cdot \left(V_r \cdot \frac{\partial V_z}{\partial r} + V_z \cdot \frac{\partial V_z}{\partial z} \right) = \mu \cdot \left[\frac{1}{r} \cdot \frac{\partial}{\partial r} \cdot \left(r \cdot \frac{\partial V_z}{\partial r} \right) + \frac{\partial^2 V_z}{\partial z^2} \right] + \rho \cdot \beta \cdot \vec{g} \cdot (T - T_m), \quad (6)$$

(d) Energy equation in the melt:

$$\rho \cdot C_p \left(V_r \cdot \frac{\partial T}{\partial r} + V_z \cdot \frac{\partial T}{\partial z} \right) = k \cdot \left[\frac{1}{r} \cdot \frac{\partial}{\partial r} \cdot \left(r \cdot \frac{\partial T}{\partial r} \right) + \frac{\partial^2 T}{\partial z^2} \right], \quad (7)$$

$$\rho \cdot C_p \cdot \frac{dT}{dt} = k \cdot \Delta T - \nabla \cdot \vec{q}_r, \quad (8)$$

where ρ is the density, V is the melt velocity, P is the pressure. The symbol μ , \vec{g} and β represent the dynamic viscosity, the gravity vector and the thermal expansion coefficient, respectively. T is the temperature, T_m is the melting temperature. C_p is the specific heat. \vec{q}_r is the vector of net radiative heat flux. In Eq.(8), the second term on the right-hand side is the divergence of the net radiative heat flux.

Table 2 Grashof number, Marangoni number, convexity of the crystal-melt interface, maximum velocity of melt near the free surface, maximum temperature of the free surface, maximum temperature of melt in Fig.2, Fig.4 and Fig.5.

Fig	Fig.2a	Fig.2b	Fig.4a	Fig.4b	Fig.5a	Fig.5b
Gr	3.5×10^5	3.5×10^5	1.2×10^5	1.2×10^5	2500	2500
Ma	0	72	0	129	0	97
H(mm)	58.3	81.5	58.8	79.6	68	53.6
Vsurmax(m/s)	5.4×10^{-3}	1.2×10^{-4}	6×10^{-4}	5.3×10^{-3}	3.7×10^{-4}	3.8×10^{-3}
Tsurmax(K)	2330.4	2332.2	2333.2	2337.6	2332.1	2334.4
Tmax(K)	2370.3	2375.2	2359	2356.3	2337.5	2337.2

2.2.3. Model of radiative heat transfer in semitransparent sapphire crystal

The approach in Ref. [15] is used to solve problems of the radiation transfer. The radiative transfer equation for a semi-transparent medium along a particular direction \vec{s} , is given as:

$$\begin{aligned} & \nabla \cdot (I_\lambda(\vec{r}, \vec{s}) \cdot \vec{s}) + (a_R + \tilde{\sigma}) \cdot I_\lambda(\vec{r}, \vec{s}) \\ & = a_R \cdot n^2 \cdot I_{b\lambda} + \frac{\tilde{\sigma}}{4\pi} \cdot \int_0^{4\pi} I_\lambda(\vec{r}, \vec{s}) d\bar{\Omega} \end{aligned} \quad (9)$$

where I is the radiation intensity which depends on position \vec{r} and direction \vec{s} , $\tilde{\sigma}$ is the scattering coefficient, $I_{b\lambda}$ is the black body intensity given by the Planck function and $\bar{\Omega}$ is the solid angle. In the study, the discrete ordinates method [16] is used to transform the equation of transfer into a set of simultaneous partial differential equations. The 4π solid angle domain at any spatial location is divided into 15×15 discrete, non overlapping solid angles and the partial differential equation for the radiative intensity in the discrete direction spanning the solid angle is obtained as Eq.(9). Hence, the radiative heat flux \vec{q}_r in Eq.(8) can be written as follows:

$$\vec{q}_r = \sum_m \omega_m \cdot (\bar{\Omega}_m \cdot \vec{n}) I_m, \quad (10)$$

where I_m is the radiative intensity for the discrete direction $\bar{\Omega}_m$, ω_m is the angular quadrature weight which sums to the surface area of the unit sphere, \vec{n} is the unit normal vector and the index is used to sum over all directions. The surface to surface model is adopted to deal with the internal radiative transport.

3. Results and discussion

Since the surface tension decreases with the temperature of melt increasing and the temperature of melt near the crucible wall is higher than that near the triple point, Marangoni convection flows from the crucible wall to the triple point. The Marangoni convection can influence the sectional flow of melt near the free surface directly and then has an impact on the global flow field and thermal field indirectly.

3.1 Effect of Marangoni convection at the shoulder turning stage

Fig.2 shows the flow field (left-hand side) and thermal field (right-hand side) during the shoulder turning stage (the length of the grown crystal is 60mm) without (a) and with (b) Marangoni convection, respectively. The thermal field and flow field in Fig.2b are different from that in Fig.2a due to the presence of Marangoni convection, which makes interface change significantly. The isotherms of Fig.2b near the axis of the flow field is nearly parallel to the axis which illustrates that the axial temperature gradient of melt is small. It can be predicted that the presence of Marangoni convection lowers the axial temperature gradient of melt which can promote the axial crystal growth, resulting in the 39.8% increase in the convexity of melt-crystal interface as shown in Table 2.

The flow field of Fig.2a and Fig.2b consists of a clockwise vortex and an anticlockwise vortex as with the results of Refs. [12, 13]. The direction of Marangoni convection is contrary to that of anticlockwise vortex near the free surface, so the anticlockwise vortex weakens and can't contact the melt-crystal interface in Fig.2b. The clockwise vortex invades the triple point region and brings the

high temperature melt to the region in Fig.2b, which increases the radial temperature gradient and suppresses the radial crystal growth near the triple point. It leads to the formation of so called temporal concave rather than remelting in Fig.3a because of its smooth surface. The temporal concave of crystal can cause stress concentration, which can increase the possibility of the formation of small-angle grain boundaries and shoulder fragmentation in Fig.3b and Fig.3c.

In the shoulder turning stage, unstable interface can cause the sticky crucible of crystal shoulder in the actual production process, so the effect of Marangoni convection on interface stability is also discussed. Fig.4 shows the temperature gradient of interface from the interface center to the triple point during the shoulder turning stage without (a) and with (b) Marangoni convection, respectively. The temperature gradient of interface in Fig.4a firstly increases and then decreases because of the contact between the anticlockwise vortex and interface in Fig.2a. But the anticlockwise vortex of Fig.2b near the free surface can't contact the interface due to the the presence of Marangoni convection, so the temperature gradient of interface increases uniformly from the interface center to the triple point in Fig.4b which makes the interface stable.



Fig.3. Sapphire crystal of Tangshan Ristal Optotech Co.,Ltd
 (a) temporal concave of crystal (b) small-angle grain boundaries of crystal
 (c) shoulder fragmentation of crystal (d) irregular remelting surface of crystal
 (e) cracking at the bottom of crystal

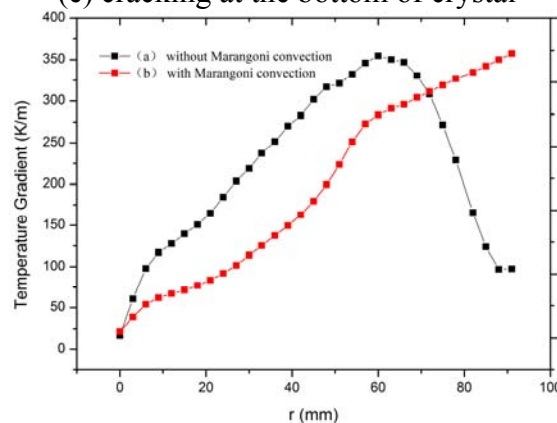


Fig.4. The temperature gradient of interface from the interface center to the triple point during the shoulder turning process without (a) and with (b) Marangoni convection

3.2 Effect of Marangoni convection at the equal-diameter stage

Fig.5 shows the flow field (left-hand side) and thermal field (right-hand side) during the equal-diameter stage (the length of the grown crystal is 120mm) without (a) and with (b) Marangoni convection, respectively. The anticlockwise vortex near the free surface exists in Fig.5a, but there is only a clockwise vortex in Fig.5b due to the Marangoni convection. Natural convection declines and

Marangoni convection strengthens relatively with the melt decreasing. When the crystal grows to half almost, the anticlockwise vortex almost disappears and the clockwise vortex exposes near the triple point. It can be found that the clockwise vortex brings the high-temperature melt to the triple point and gives rise to the remelting of Fig.3d by observing the isotherms and flow lines in Fig.5b. Since the ratio of Gr and Ma is 930.2 as shown in Table 2, the remelting is mainly caused by natural convection. The larger convexity of melt-crystal interface in Fig.5b reduces the volume of melt flow, which makes the isotherms more distorted than that in Fig.5a. The more distorted isotherms increases the heat flux to the triple point region and then aggravates the remelting. The remelting begins in the middle of crystal surface in Fig.3d, which conforms to the simulation results.

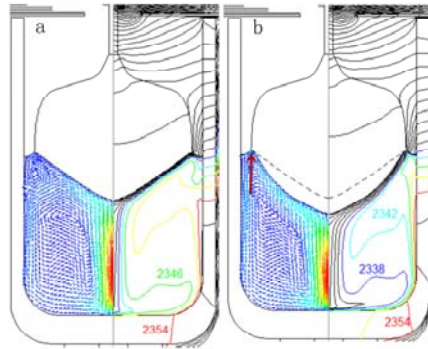


Fig.5. The flow field (left-hand side) and thermal field(right-hand side) during the equal-diameter stage (the length of the grown crystal is 120mm) without (a) and with (b) Marangoni convection

3.3 Effect of Marangoni convection at the last stage

Fig.6 shows the flow field (left-hand side) and thermal field (right-hand side) during the last stage (the length of the grown crystal is 230mm) without (a) and with (b) Marangoni convection, respectively. The direction of Marangoni convection is the same as that of the clockwise vortex in Fig.6a, which makes the maximum flow velocity of melt near the triple point increase from 3.7×10^{-4} m/s in Fig.6a to 3.8×10^{-3} m/s in Fig.6b as shown in Table 2. The strength of natural convection and Marangoni convection are an order of magnitude difference due to the ratio 25.8 of Gr and Ma as shown in Table 2. The characteristic size K and the characteristic size L are in the vertical direction, so the flow velocity variation and the ratio of Gr and Ma are considered comprehensively. It can be concluded that the contribution of Marangoni convection on the heat transfer dominates at the last stage. The remelting of the last stage in Fig.3d is mainly caused by Marangoni convection.

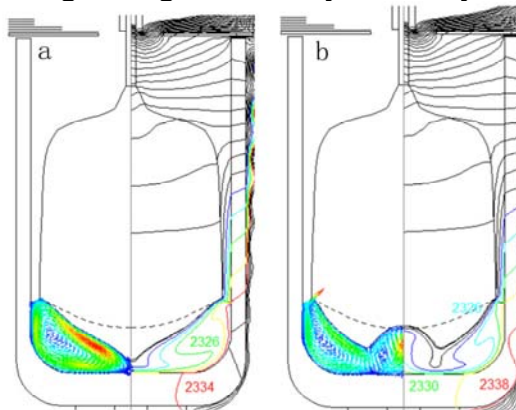


Fig.6. The flow field (left-hand side) and thermal field (right-hand side) during the last stage (the length of the grown crystal is 230mm) without (a) and with (b) Marangoni convection

In the last crystal growth stage, the effect of Marangoni convection on melt-crystal interface is more obvious. Comparing the ratio of Gr and Ma in Fig.2b and Fig.6b, it can be found that the strength of Marangoni convection relatively increases due to almost unchanged surface of melt and greatly decreasing volume of melt with the crystal growing. Since the direction of Marangoni convection is the same as that of the vortex in Fig.6a, the strength of the vortex near the free surface increases,

which turns one vortex in Fig.6a into two vortices in Fig.6b. The main vortex in Fig.6b compresses the weak vortex to the bottom of crystal which causes the melt-crystal interface inversion. The interface inversion increases the dislocation density and the thermal stress of crystal [17], which brings about the cracking at the bottom of crystal as shown in Fig.3e.

4. Conclusions

The influence of Marangoni convection on thermal field, flow field and melt-crystal interface is studied. The presence of Marangoni convection increases the convexity of interface by 39.8% and influences flow pattern which causes the temporal concave of crystal during the shoulder turning process. The temperature gradient of interface increases uniformly from the interface center to the triple point which makes the interface stable due to Marangoni convection. The clockwise vortex exposes near the triple point which leads to the beginning of remelting and Marangoni convection aggravates the remelting at the equal-diameter stage. During the last stage, Marangoni convection reinforces the main vortex near the free surface greatly which turns one vortex into two vortices and gives rise to interface inversion. The interface inversion increases the dislocation density and the thermal stress of crystal, which brings about the cracking at the bottom of crystal. The numerical simulation results agree well with the experiment photo.

References

- [1] S. Toru and Z. Sakae, *J. Appl. Phys.* 61, 2533-2541 (1987).
- [2] G.G. Wang, M.F. Zhang, J.C. Han, X.D. He, H.B. Zuo and X.H. Yang, *Cryst. Res. Technol.* 43, 531-536 (2008).
- [3] M.S. Akselrod and F.J. Bruni, *J. Cryst. Growth* 360, 134-145 (2012).
- [4] M.H. Tavakoli, T.A. Abasi, S. Omid and E. Mohammadi-Manesh, *Cryst. Res. Technol.* 48, 58-68 (2013).
- [5] H.S. Fang, S.Wang, Z.L. Jin, J. Tian and J.F. Xu, *Cryst. Res. Technol.* 48, 649-657 (2013).
- [6] C.H. Xu, M.F. Zhang, S.H. Meng, J.C. Han, G.G. Wang, and H.B. Zuo, *Cryst. Res. Technol.* 42, 751-757 (2007).
- [7] C. Chen, H.J. Chen, W.B. Yan, C.H. Min, H.Q. Yu, Y.M. Wang, P. Cheng and C.C. Liu, *J. Cryst. Growth* 388, 29-34 (2014).
- [8] G. Samanta, A. Yeckel, P. Daggolu, H.S. Fang, E.D. Bourret-Courchesne and J.J. Derby, *J. Cryst. Growth* 335, 148-159 (2011).
- [9] W.J. Lee, Y.C. Lee, H.H. Jo and Y.H. Park, *J. Cryst. Growth* 324, 248-254 (2011).
- [10] <<http://www.semitech.us>>
- [11] M.H. Tavakoli, *Cryst. Res. Technol.* 310, 3107-3112 (2008).
- [12] S.E. Demina, E.N. Bystrova, M.A. Lukanina, E.V. Eskov, M.V. Nikolenko, D.A. Marshanin, V.S. Yuferev and V.V. Kalaev, *Opt. Mater.* 30, 62-65 (2007).
- [13] S.E. Demina, E.N. Bystrova, V.S. Postolov, V.M. Mamedov, V.S. Yuferev, E.V. Eskov, M.V. Nikolenko, V.S. Postolov and V.V. Kalaev, *J. Cryst. Growth* 310, 1443-1447 (2008).
- [14] D.P. Lukanin, V.V. Kalaev, Yu.N. Makarov, T. Wetzel, J. Virbulis and W. Von Ammon, *J. Cryst. Growth* 266, 20-27 (2004).
- [15] S.A. Rukolaine, M.G. Vasilyev, V.S. Yuferev and V.M. Mamedov, *JQSRT* 84, 371-382 (2004).
- [16] S.E. Demina and V.V. Kalaev, *J. Cryst. Growth* 320, 23-27 (2011).
- [17] A.V. Denisova, V.T. Gabrielyan, J.O. Punin, O.S. Grunsky and N.A. Sennova, *J. Cryst. Growth* 275, 697-701 (2005).